water

MDPI

Article

Thermal Polymerisation Synthesis of g-C_3N_4 for Photocatalytic Degradation of Rhodamine B Dye under Natural Sunlight

Muxi Zhang [1,2,3], Meiyan Xing [4], Bin Dong [1,2,3,4], Hongxia Zhang [1,2,3,*], Xiaojie Sun [1,2,3,*], Qiuhong Li [1,2,3], Xueshuang Lu [1,2,3], Jingjing Mo [1,2,3] and Hongxiang Zhu [5]

1 College of Environmental Science and Engineering, Guilin University of Technology, Guilin 541006, China; zhangmuxi2022@163.com (M.Z.); dongbin@tongji.edu.cn (B.D.); m18868006306@163.com (Q.L.); 17344519765@163.com (X.L.); 18579411886@163.com (J.M.)
2 Guangxi Key Laboratory of Environmental Pollution Control Theory and Technology, Guilin University of Technology, Guilin 541006, China
3 Guangxi Collaborative Innovation Center for Water Pollution Control and Water Safety in Karst Area, Guilin University of Technology, Guilin 541006, China
4 School of Environmental Science and Engineering, Tongji University, Shanghai 200092, China; xingmeiyan@tongji.edu.cn
5 Modern Industry College of Ecology and Environmental Protection, Guilin University of Technology, Guilin 541006, China; zhx@gxu.edu.cn
* Correspondence: zhx75@glut.edu.cn (H.Z.); sunxiaojie@glut.edu.cn (X.S.); Tel.: +86-1507-8329-789 (X.S.)

Abstract: The photocatalytic performance of g-C_3N_4 materials prepared by different precursors for Rhodamine B (RhB) dye degradation was studied. Their crystal structure, morphologies, chemical compositions, functional groups, and optical and photoelectrochemical performances of prepared g-C_3N_4 were analysed and characterised using X-ray diffraction, scanning electron microscopy, X-ray photoelectron spectroscopy, Fourier transform infrared spectroscopy, UV-Vis diffuse reflectance spectra, photoluminescence, and electrochemical workstations. The degradation of RhB dye in the presence of visible light and sunlight was utilised to assess the photocatalytic efficiency of the g-C_3N_4 photocatalyst. The results of the photocatalytic comparison experiment showed that the g-C_3N_4 photocatalyst prepared with urea as a precursor (UCN) has the best photocatalytic performance, achieving 99.61% removal in 40 min. In addition, the photocatalyst UCN can completely degrade 10 mg/L RhB dye within 20 min under sunlight, demonstrating its potential for practical applications under natural sunlight conditions. After four cycles, the degradation rate remains above 99%, demonstrating excellent stability and reusability. Due to its lower average pore number, larger BET-specific surface area and volume of pores, UCN provides more activity spaces and facilitates the adsorption of pollutant molecules, thereby enhancing photocatalytic activity. It was established through the active substance trapping studies that the main reactive species involved in the photocatalytic degradation process of RhB dye is $\bullet O_2^-$. This study showed that g-C_3N_4 synthesised with urea as the precursor has better photocatalytic performance in the degradation of RhB dye.

Keywords: g-C_3N_4; urea; melamine; photocatalysts; Rhodamine B

check for updates

Citation: Zhang, M.; Xing, M.; Dong, B.; Zhang, H.; Sun, X.; Li, Q.; Lu, X.; Mo, J.; Zhu, H. Thermal Polymerisation Synthesis of g-C_3N_4 for Photocatalytic Degradation of Rhodamine B Dye under Natural Sunlight. *Water* **2023**, *15*, 2903. https://doi.org/10.3390/w15162903

Academic Editor: Mehrab Mehrvar

Received: 8 July 2023
Revised: 31 July 2023
Accepted: 9 August 2023
Published: 11 August 2023

1. Introduction

With the continuous advancement of China's industrialisation and urbanisation, environmental pollution, such as water pollution, has become an increasingly severe problem, a crucial factor restricting economic development and social progress [1]. Many efforts have been made to eliminate contaminants from the water. Recently, photocatalysis technology was investigated for removing organic dyes from water because of its mild reaction conditions, low price, cleanliness, and high efficiency [2,3]. Budnyak et al. [4] synthesised the photoactive lignin/$Bi_4O_5Br_2$/BiOBr bioinorganic complex site and found that 18.9% of

$Bi_4O_5Br_2$/BiOBr exhibited photocatalytic degradation capabilities towards cationic methylene blue and Rhodamine B (RhB) dyes under 20 W blue light irradiation. Li et al. [5] fabricated a C-BiOCl composite photocatalyst and found that it exhibited superior photocatalytic activity with RhB dye degradation irradiated for only 6 min under a 300 W Xe arc lamp. Zhang et al. [3] synthesised ZSM-5/$Bi_4O_5Br_2$ photocatalysts and found that 1ZSM-5/$Bi_4O_5Br_2$ had an excellent photocatalytic performance. The RhB dye removal rate reached 99.86% within 25 min under 300 W Xe arc lamp irradiation. Yang et al. [6] synthesised a nitrogen-deficient porous g-C_3N_4 photocatalyst that can completely degrade RhB dye in just 20 min under simulated visible light irradiation.

The photocatalytic process depends on highly active substances, such as superoxide radicals ($\bullet O_2^-$), hydroxyl radicals ($\bullet$OH), and holes (h^+) produced by the photocatalyst after absorbing light energy to decompose target pollutants [7]. Various photocatalysts, including TiO_2-based [8], Bi-based [9,10], Mo-based [11], Zn-based [12], and Ag-based [13] semiconductors, have been developed and effectively removed RhB dye. Nevertheless, many of the aforementioned photocatalysts might give off precious elemental metals, introducing the risk of additional contamination caused by the release of metals from the photocatalysts. Therefore, metal-free photocatalysts are environmentally friendly alternatives that have prospective widespread usage [14].

Graphite carbon nitride (g-C_3N_4) has generated considerable interest as a metal-free photocatalyst because of its straightforward and affordable synthesis; energy bandwidth for solar power collection; thermal stability; trustworthy chemical inertness; and electrochemical, multipurpose, and nicely organised photocatalytic characteristics [15–17]. g-C_3N_4 has the in-plane tri-s-triazine units, and the sp^2-hybridised carbon and nitrogen form a π-conjugated system, advantageous for modifying materials based on nanosheets in electrical and optical electronics [18,19]. g-C_3N_4 has good photocatalytic performance because of the narrow band gap and capacity to take in light that is visible, which can effectively absorb and use the light of wavelengths below 460 nm [20]. The g-C_3N_4 band gap is approximately 2.70 eV, and the conduction band (CB) potential is negative (−1.3 eV), providing a strong reduction ability for photogenerated electrons [21]. The synthesis methods of g-C_3N_4 primarily include deposition [22,23], template [24], solvothermal [25], and thermal polymerisation [26,27]. Thermal polymerisation is frequently employed because of its affordable, easy availability of raw materials, and simple operation. A few molecules with a high nitrogen content, such as cyanamide [28], dicyandiamide [29], melamine [30], and urea [31], served as a single source of molecular antecedents to fabricate g-C_3N_4. Ma et al. [32] prepared g-C_3N_4 from various raw materials using thermal polycondensation, and the shapes of the products obtained using mono-cyanamide, dicyandiamide, and melamine were spherical, irregular, and layered, respectively. Liu et al. [33] prepared 3D interconnected g-C_3N_4 via one-step thermal polymerisation using melamine and cyanuric acid.

The occurrence of catalytic reactions necessitates adsorption, and numerous studies have highlighted that optimal adsorption can yield enhanced catalytic efficiency [34,35]. Zhang et al. [36] loaded Cu on an oxide semiconductor surface to improve wastewater remediation, and the results showed that Cu particle deposition can improve the adsorption activity of a single oxide and thus improve the photocatalytic activity. Luo et al. [37] demonstrated that the adsorption process promotes the photodegradation of pollutants by g-C_3N_4, while the photodegradation of dyes supported on g-C_3N_4 regenerates its adsorption capacity many times, indicating that the photocatalytic process also enhances pollutant adsorption on g-C_3N_4. Yu et al. [38] confirmed that a modified g-C_3N_4/MgZnAl-calcined layered double hydroxide composite (MCN/cLDH) possesses a large S_{BET}-specific surface area, which enhances its adsorption capacity and improves the separation efficiency of photogenerated carriers. Furthermore, MCN/cLDH nanostructures exhibit enhanced synergistic degradation through adsorption-photocatalysis to remove oxytetracycline (95.73%) from artificial seawater. Ni et al. [39] demonstrated that the addition of g-C_3N_4 to CCN (Co_3O_4 QDs/3D g-C_3N_4) catalyst led to an increase in tetracycline adsorption, indicating that an optimal amount of g-C_3N_4 as a Co_3O_4 QDs carrier can enhance adsorption and

expose more active sites, thereby achieving the best synergistic effect between adsorption and oxidative degradation. Liu et al. [40] prepared an efficient three-dimensional (3D) hollow porous C-doped polymeric carbon nitride (CPCN) catalyst, and found that the formed 3D hollow porous structure gave the CPCN catalyst a large specific surface area and numerous exposed active sites, promoted the substrate adsorption reaction and maintained its structural stability, and thus improved its photolytic water hydrogen production and pollutant elimination activity.

In this study, melamine and urea were utilised as precursors for the preparation of g-C_3N_4 (MCN and UCN, respectively) through thermal polymerisation. The photocatalytic degradation ability and practical application potential of MCN and UCN were assessed by comparing the change in RhB dye concentration under visible light and sunlight irradiation. The crystal structure, morphology, chemical composition, functional groups, optics, photoelectric chemical properties, and stability of g-C_3N_4 were investigated. To understand how RhB molecules behaved in the reaction procedure, three-dimensional excitation-emission matrix fluorescence spectra (3D EEMs) were used. In comparison to MCN, UCN has better photocatalytic capabilities for degrading RhB dye when exposed to visible light and sunlight. This study serves as a reference for research on the synthesis and properties of g-C_3N_4.

2. Experimental

2.1. Materials

Urea (H_2NCONH_2), melamine ($C_3H_6N_6$), isopropanol (C_3H_8O, IPA), benzoquinone ($C_6H_4O_2$, BQ), Rhodamine B (RhB, $C_{28}H_{31}ClN_2O_3$), and sodium oxalate ($Na_2C_2O_4$, SO) were purchased from Xilong Scientific Co., Ltd. (Shantou, China). All reagents are analytical grade and can be used without further purification.

2.2. Synthesis of g-C_3N_4

g-C_3N_4 was synthesised using the thermal polymerisation process with melamine and urea as the reactive precursors, and 15 g melamine and urea were placed, respectively, into a 50 mL covered crucible in a muff furnace. The heating rate was set to 5°/min; the target temperature was 550 °C, maintained for 3 h; and the substance was ground for 5 min to obtain g-C_3N_4 photocatalytic materials, named MCN and UCN.

2.3. Material Characterisation

The crystal structure information of MCN and UCN was recorded using powder X-ray diffraction (XRD) on a PANalytical X'Pert^3 Powder diffraction instrument. The specific functional groups of MCN and UCN were measured using Fourier transform infrared spectroscopy (FTIR) (IS10, Thermo Fisher Scientific, Madison, WI, USA), and the morphology and structure were evaluated using scanning electron microscopy (SEM) (JSM-7900F Plus, Nidec Corporation, Kyoto, Japan). The surface chemical composition and electronic state of MCN and UCN were determined using X-ray photoelectron spectroscopy (XPS) (Thermo Scientific K-Alpha Nexsa, Waltham, MA, USA), and the N_2 adsorption–desorption isotherms and Brunauer–Emmett–Teller (BET) surface area were evaluated using a specific surface area analyser (ASAP 2460). The optical properties were obtained using diffuse reflectance spectra (DRS) via a 3600 UV-Vis spectrophotometer. The photoluminescence (PL) spectra of MCN and UCN were studied using an FLS 980 fluorescence spectrophotometer (Edinburgh Instruments, Livingston, UK) employing an excitation wavelength of 325 nm. Electrochemical impedance (EIS) and photocurrent response tests were conducted on MCN and UCN using an electrochemical workstation (CHI660E, Shanghai Chenhua Instrument Co., Ltd., Shanghai, China). A standard three-electrode system is adopted (sample-coated conductive glass is the working electrode, platinum electrode is the opposite electrode, and Ag/AgCl is the reference electrode). The working electrode is prepared as follows: 10 mg of powder sample is weighed and dispersed in 1 mL of ethanol solution, followed by the addition of 50 μL of Nafion solution. The mixture is then subjected to ultrasonic

treatment for 30 min to achieve a homogeneous suspension. Subsequently, 150 µL of the suspension is dropped onto an ITO glass substrate and dried at room temperature for testing. The measurement process was conducted in a 0.1 M Na_2SO_4 aqueous solution. Raman analysis was performed using a confocal Raman microscope (CRM) (Alpha300R, WITec GmbH, Ulm, Germany) equipped with a TEM single-frequency laser (λ = 532 nm, laser power = 40 mW, WITec GmbH, Germany). Elemental analysis of MCN and UCN was performed using the PerkinElmer 24,000 Series II CHNS/O analyser. The EEM fluorescence spectrum was acquired using a fluorescence spectrophotometer (Aqualog-UV-800).

2.4. Photocatalytic Performance Measurement

The photocatalytic performance was assessed by comparing the photocatalytic degradation of RhB dye (dissolved in deionised water) using MCN and UCN. The procedure was as follows: 50 mg of MCN (or UCN) was weighed and placed into a solution in a 250 mL beaker (100 mL, 10 mg/L, 20 mg/L, and 30 mg/L RhB dye). To ensure a balance between adsorption and desorption, each suspension was agitated in the darkness for 60 min and then exposed to a 300 W Xenon lamp (λ ≥ 420 nm) or direct sunlight. Experiments using sunlight illumination were carried out outside between 13:00 pm and 14:00 pm (2023/5; weather: fine; 26–35 °C). During the photocatalytic procedure, 5 mL of suspension was taken at predetermined time intervals, and the photocatalyst powder was separated using a 0.45 µm filter membrane. The RhB dye concentration (λ_{max} = 554 nm) in the suspension at different irradiation time intervals was measured using a 6100A UV-Vis spectrophotometer (Shanghai Yuanxi Instruments Co., Ltd., Shanghai, China), and the Lambert–Beer law was used to calculate the RhB removal efficiency.

3. Results and Discussions

3.1. Crystal Structure and Functional Group Analysis

The crystal properties and composition of the synthesised photocatalysts were characterised using the XRD technique. The diffraction pattern in Figure 1a displays two distinct peaks at 2θ values of 13.18° and 27.86°, which can be attributed to the (100) and (002) planes of g-C_3N_4, respectively (JCPDS NO. 01-087-1526) [41]. The (100) crystal plane indicates the periodic arrangement of the structural units in the layer, and the (002) crystal plane corresponds to the interlayer stacking of aromatic segments. The positions of these two diffraction peaks correlate with those previously reported for g-C_3N_4 [42]. Compared with MCN, UCN's peak intensity and width of the (002) crystal plane is weaker and broader, indicating that urea as a precursor can inhibit the crystal growth of g-C_3N_4. The average crystal diameters were calculated using Scherrer's equation: D = Kλ/βcosθ, where D is the average crystal diameter (nm); K is the Scherrer constant (0.89); λ is the wavelength of the X-ray (1.5406°A); β is the full width at half-maximum intensity and θ corresponds to the angle of maximum peak [3,43], and the calculated average crystallite sizes of MCN and UCN are equal to 3.67 and 1.77 nm, respectively.

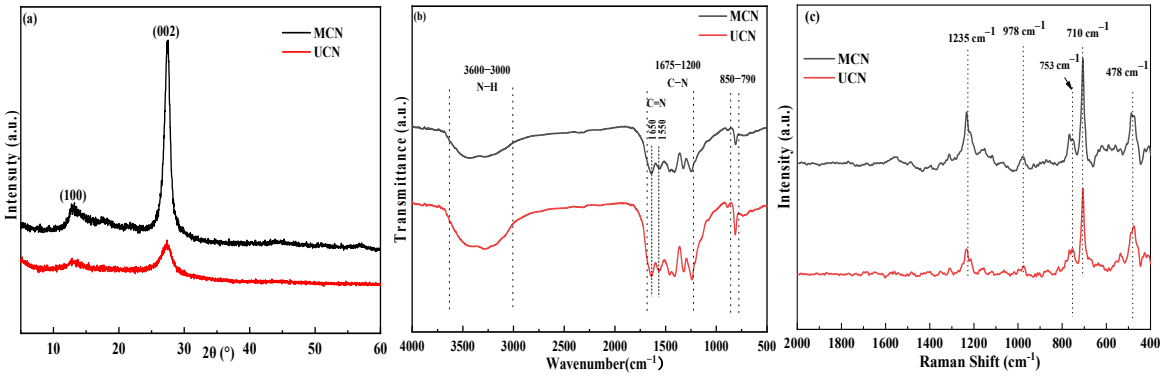

Figure 1. (**a**) XRD patterns, (**b**) FTIR spectra, and (**c**) Raman spectra of MCN and UCN.

The intrinsic chemical structure of the samples can be detected using FTIR spectra. Figure 1b shows that the characteristic peak value at 810 cm^{-1} corresponds to the out-of-plane bending vibration of the triazine ring [44], and the broader band of approximately 3000 to 3600 cm^{-1} corresponds to the N–H stretching vibration [45]. The characteristic band at 1675–1200 cm^{-1} ascribes to the stretching vibration mode of C–N and C=N [46,47]. The tensile vibrations of the bonds in the prepared photocatalyst can be revealed via Raman spectroscopy, as depicted in Figure 1c. The peaks observed at 478 cm^{-1}, 710 cm^{-1}, 753 cm^{-1}, 978 cm^{-1}, and 1235 cm^{-1} correspond to the tensile vibrations of C–C and C–N heterocycles [48–50].

3.2. Microstructure and Compositions Analysis

SEM was performed on MCN and UCN to study the typical morphology and detailed structure of the as-prepared samples. Figure 2a shows that MCN presents a hierarchical structure with layers stacked tightly into blocks. UCN becomes thinner and presents a more dispersed and uniform porous structure (Figure 2c). The degree of the UCN sample's interlayer stacking structure is low, and the interlayer structure is loose, which can increase the surface area and reactive sites [51]. The results are consistent with those of BET. SEM-EDS was used to analyse the distribution and content percentage of elements on the surface of the photocatalyst. C and N are uniformly distributed on the surface of the photocatalyst (Figure 2b,d). The results of the elemental analysis of MCN and UCN are shown in Table 1. The C/N of MCN and UCN are 0.56 and 0.61, respectively.

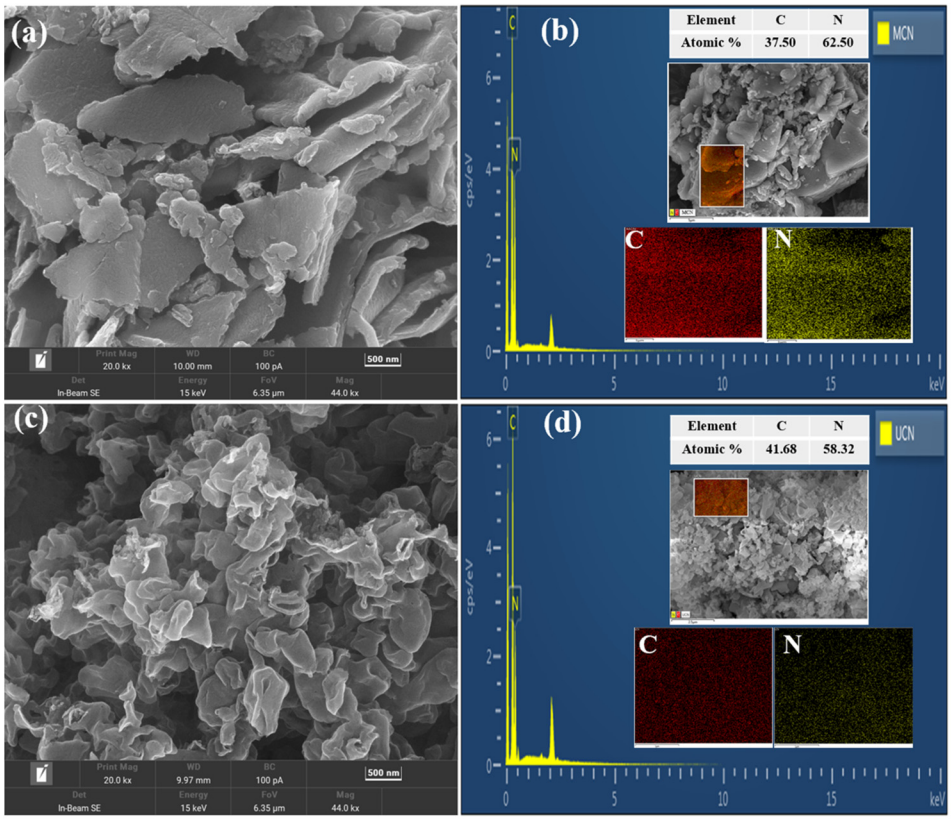

Figure 2. SEM patterns of (**a**) MCN and (**c**) UCN; EDS mapping images of (**b**) MCN and (**d**) UCN.

Table 1. Elemental analysis of MCN and UCN.

Samples	C (%)	N (%)	C/N
MCN	33.93	60.97	0.56
UCN	34.73	57.32	0.61

XPS was used to analyse and compare the surface elemental composition of MCN and UCN. The XPS survey spectrum shows that C and N existed in MCN and UCN (Figure 3a). The C 1s spectra are fitted into two peaks at 288.1 and 284.8 eV (Figure 3b). The primary C 1s peak at 288.1 eV is associated with the sp^2-bonded carbon (N–C=N), and the peak at 284.8 eV corresponds to C–C [31]. The N1s XPS spectrum in Figure 3c displays four peaks at 398.5, 400.4, 401.3, and 404.2 eV [52]. These peaks correspond to C=N–C, ternary N ($N(–C)_3$), N-H bond [7,46], and π-excitations [31], respectively.

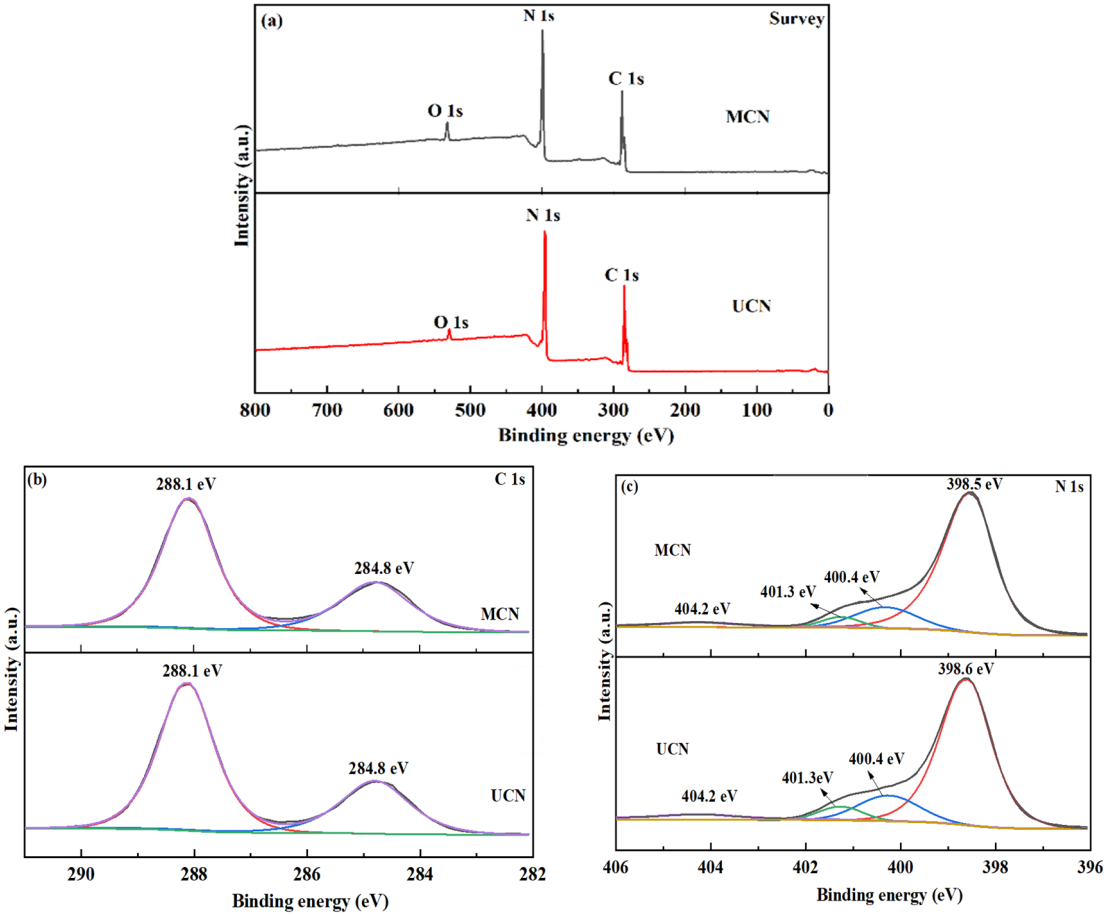

Figure 3. XPS spectra: (**a**) survey scan, (**b**) C 1s, and (**c**) N 1s of MCN and UCN.

3.3. BET Surface Area and Pore Size Distribution Analysis

The BET surface area and the distribution of pore sizes for the MCN and UCN were measured using the N_2 adsorption–desorption isotherms (Figure 4). The adsorption–desorption isotherms of the MCN and UCN are classical type IV with a hysteresis loop of type H_3, indicating that the catalyst has a mesoporous structure [53]. The BET surface area of UCN is 60.03 $m^2 \cdot g^{-1}$, more than eight times that of MCN. Table 2 shows that UCN exhibits a larger specific surface area, greater pore volume, and smaller average pore size, thereby providing an increased number of active sites that contribute to the adsorption of pollutant molecules [54]. Therefore, the mesoporous structure and large BET surface area of UCN are expected to enhance the adsorption capacity and photocatalytic degradation efficiency of pollutants.

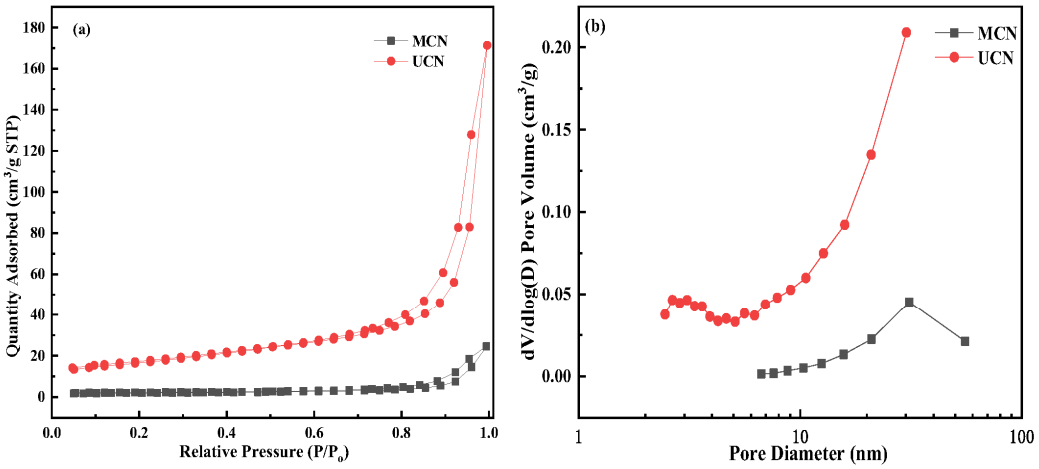

Figure 4. (**a**) N_2 adsorption–desorption isotherms and (**b**) pore size distribution curves of MCN and UCN.

Table 2. The results of the N_2 adsorption–desorption analysis for MCN and UCN.

Samples	BET Surface Area ($m^2 \cdot g^{-1}$)	Pore Volume ($cm^3 \cdot g^{-1}$)	Average Pore Size (nm)
MCN	7.4408	0.002278	20.4142
UCN	60.0322	0.005151	17.6493

3.4. UV–Vis Spectroscopy and Photochemical Characteristics

To understand the light absorption capacity of MCN and UCN, UV–vis absorption spectra were analysed, as shown in Figure 5. The sharp innate absorption edge for MCN and UCN are at around 480 and 460 nm, respectively. The absorption edge's shift is primarily due to the porous structure's strong quantum constraint causing the nanosheets to become thinner and smaller in the UCN [55]. The Kubelka–Munk formula was used for estimation to understand the MCN and UCN energy bands better. This is based on $\alpha h\upsilon = A\ (h\upsilon - Eg)^{n/2}$, where a, h, n, A and *Eg* are the absorption coefficient, the Planck constant, light frequency, a constant and band gap energy [56], respectively. The value of n depends on the type of optical transition exhibited by the semiconductor. For g-C_3N_4 with a direct band gap, the value of n is equal to 1 [21,57]. The *Eg* of MCN and UCN are 2.70 and 2.79 eV, respectively, similar to the study by Hong et al. [58].

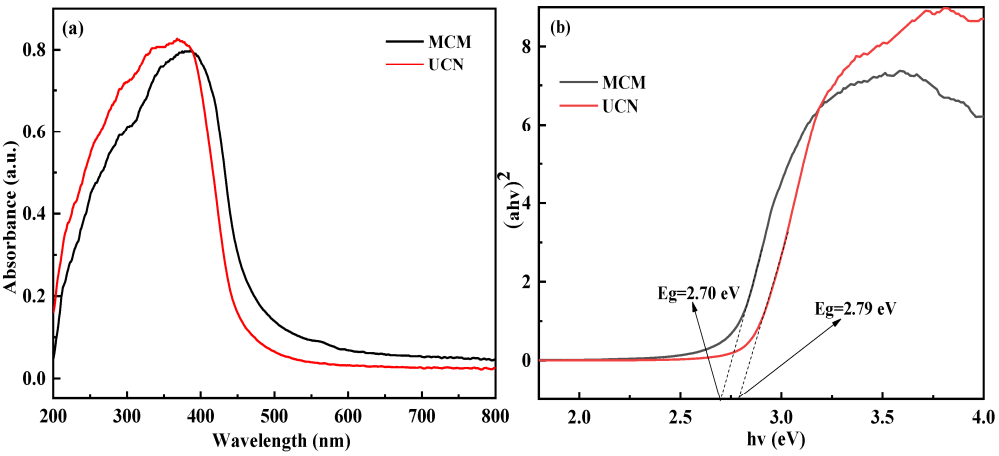

Figure 5. (**a**) UV-vis diffuse reflectance spectra and (**b**) plots of $(\alpha h\upsilon)^2$–hυ of MCN and UCN.

Recombining photogenerated carriers within the photocatalyst releases fluorescence energy, and a high fluorescence signal indicates a high photogenerated carrier recombina-

tion rate [9,54]. Therefore, PL analysis was used to evaluate the efficiency of photogenerated electron–hole pair separation. Figure 6a shows that MCN and UCN have distinct signal peaks near 480 nm. The UCN fluorescence intensity is significantly weaker than that of MCN, indicating that UCN aids in the separation of photogenerated electron-hole pairs and thus improves photocatalytic activity. Furthermore, the photocarrier interface separation and migration of g-C_3N_4 were measured using the Nyquist plots of EIS. Generally, a smaller radius of the arc on the EIS Nyquist plot indicates more efficient interface charge transfer and lower photogenerated electron–hole pair recombination [59]. In Figure 6b, the EIS Nyquist plot of UCN shows a smaller arc radius than that of MCN, indicating that UCN has a lower interfacial charge transfer resistance and can separate photoinduced carriers more efficiently. The photocurrent responses of MCN and UCN are shown in Figure 6c. The higher the photocurrent density, the better the electron–hole pair separation performance [60]. The photocurrent response of UCN is higher, which further indicates that UCN has a stronger electron–hole pair separation ability.

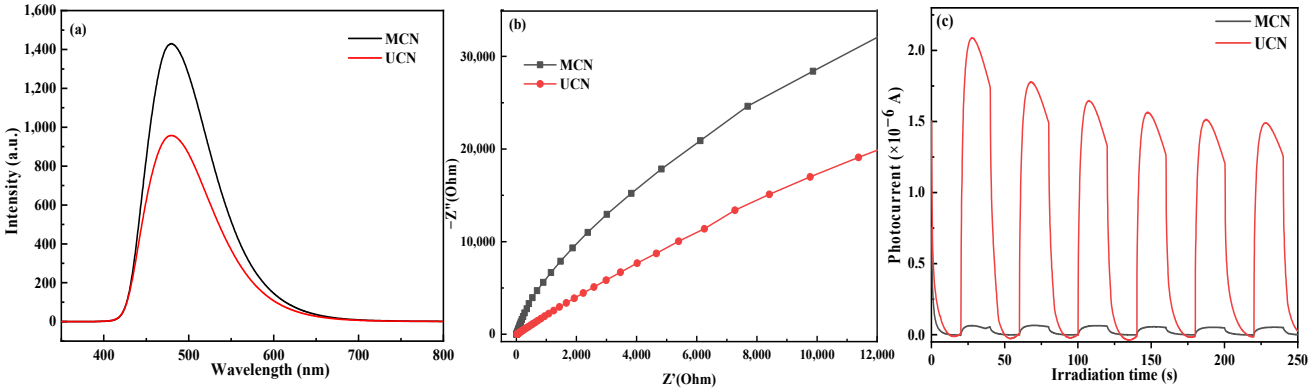

Figure 6. (**a**) PL spectra, (**b**) EIS plots, and (**c**) photocurrent responses of MCN and UCN.

3.5. Photocatalytic Degradation Performance

The degradation of RhB dye was used to gauge both the adsorption and photocatalytic abilities of MCN and UCN. Figure 7 demonstrates that UCN exhibits superior removal efficiency in treating RhB dye at different concentrations under visible light or sunlight, with equilibrium being achieved within 20 min. After 40 min of visible light exposure (Figure 7a), the removal efficiency of UCN towards 30 mg/L RhB dye reaches up to 99.61%, which is higher by 20.31% compared to MCN. MCN has the best effect on the treatment of RhB dye with a concentration of 10 mg/L under visible light, and the removal rate is 98.58% after 40 min of illumination, but the removal efficiency is still lower than that of UCN (99.36%). Additionally, the applicability of the prepared photocatalyst under natural sunlight was also investigated. As shown in Figure 7c, the photocatalyst UCN outperforms the laboratory-simulated visible light catalytic system by completely degrading 10 mg/L of RhB dye in 20 min. This is mostly because that natural sunlight emits not only visible light but also ultraviolet radiation, which can potentially enhance the generation of charge carriers by the catalyst and facilitate the degradation of RhB dye [61]. In order to visualise the photocatalytic degradation of RhB dyes via UCN and MCN, a degradation diagram excluding the adsorption effect was made. As shown in Figure 7b,d, under simulated visible light and real sunlight irradiation, the effect of UCN is still better after deducting the adsorption effect, which indicates the adsorption–photocatalytic synergy. In conclusion, the utilisation of urea yields superior results in the preparation of g-C_3N_4.

Figure 8 shows the UV-Vis absorption spectra for the photodegradation of RhB dye in the UCN photocatalyst. The maximum absorption peak of RhB dye at 554 nm (λ_{max}) gradually decreased with the photodegradation process. After 5 min of visible light irradiation, the UCN photocatalyst decomposed approximately 96.15% of the RhB dye. The primary absorption peak's position was significantly reduced, indicating that UCN has excellent photocatalytic performance.

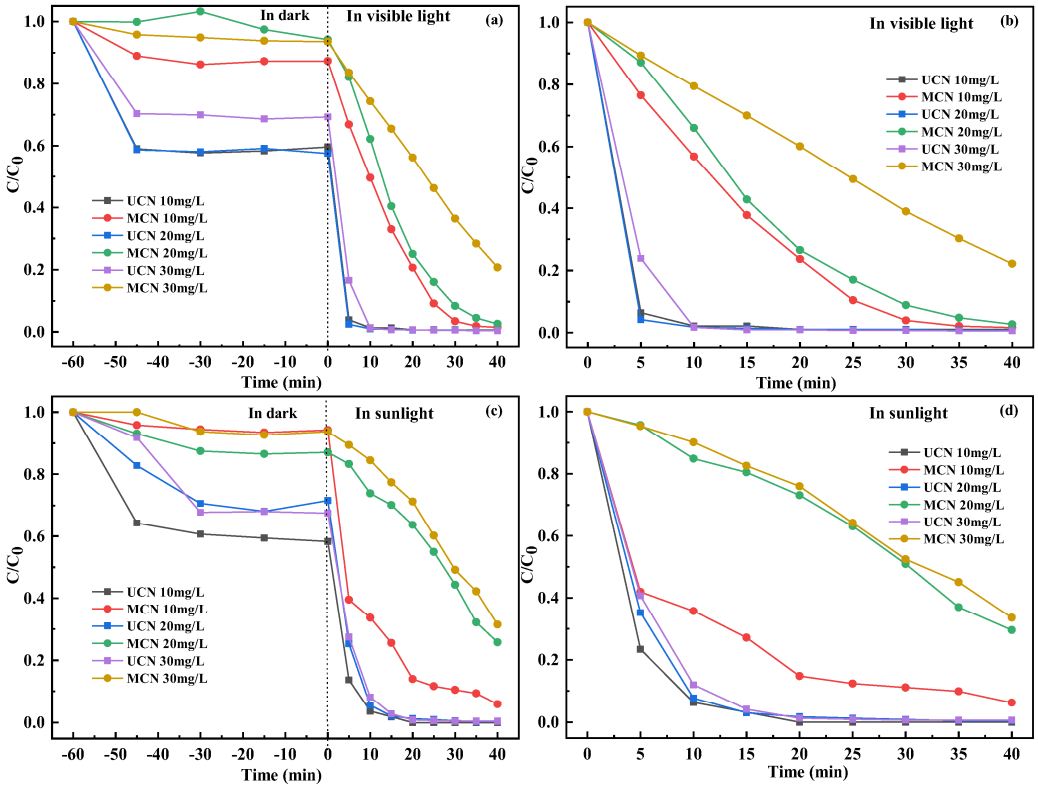

Figure 7. (**a**) Adsorption and photocatalytic degradation, (**b**) photocatalytic degradation of RhB dye under visible light; (**c**) adsorption and photocatalytic degradation, (**d**) photocatalytic degradation of RhB dye under sunlight.

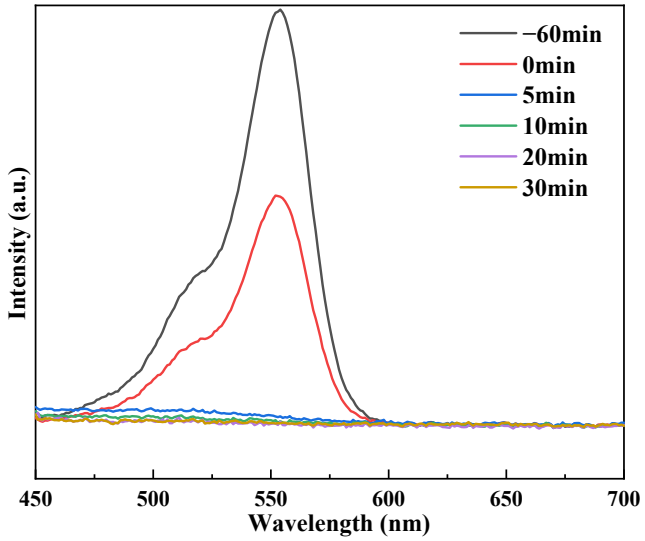

Figure 8. UV-Vis spectral changes of RhB dye in UCN.

In addition, 3D EEMs technology was employed to elucidate the alterations of RhB dye after photocatalysis. Before visible light illumination, the characteristic fluorescence signal appeared at Ex/Em = 460–590/540–700 nm and 200–425/550–670 nm. After being stirred in darkness for 30 min (Figure 9a), the position and shape of the fluorescence peak remained relatively stable, but its intensity slightly decreased, indicating that the RhB molecule was only adsorbed on the catalyst without decomposition. After 40 min, the fluorescence intensity began to decrease. This indicates that the RhB has broken down into pieces and molecular fragments [62]. This is consistent with the results shown in Figure 8.

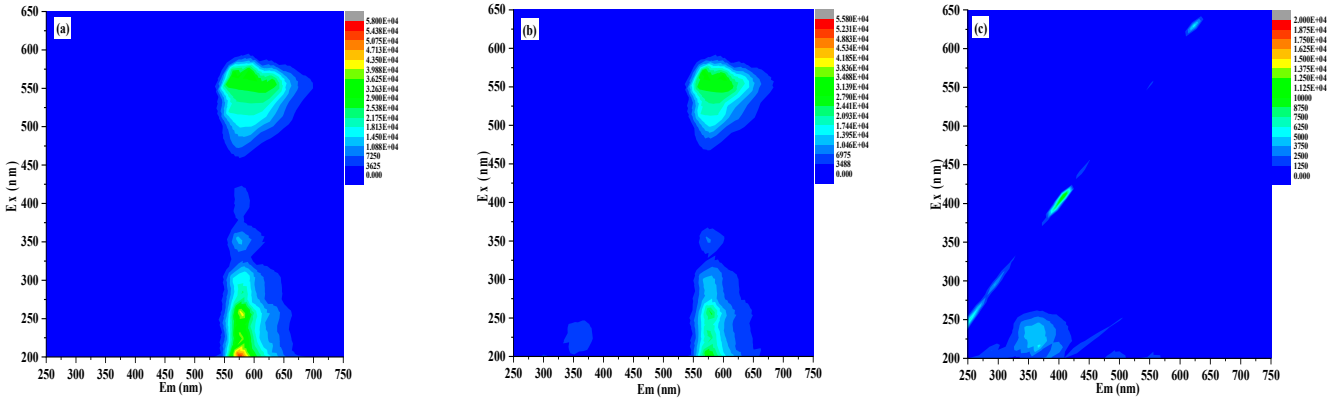

Figure 9. The 3D EEMs results of the RhB solution: (**a**) the original solution, (**b**) after dark adsorption for 60 min, and (**c**) after illumination for 40 min of UCN.

The stability and recycling properties of the UCN were verified by carrying out four cycle tests for the photocatalytic degradation of RhB dye. After each photocatalytic degradation, the powder material was extracted and recycled, cleaned three times with deionised water, and dried for the next cycle experiment. Compared with the first time (99.61%), the removal rate shows a slight change (Figure 10a). In four cycles, the treatment rates were 99.58%, 99.49%, 99.36%, and 99.35%. The results indicate that UCN exhibits exceptional stability and reusability. The photostability of UCN was further confirmed by measuring the XRD patterns of UCN after four recycling tests on RhB (Figure 10b). The XRD results show that there was no change in the crystal structure of UCN and that all the characteristic peaks are present.

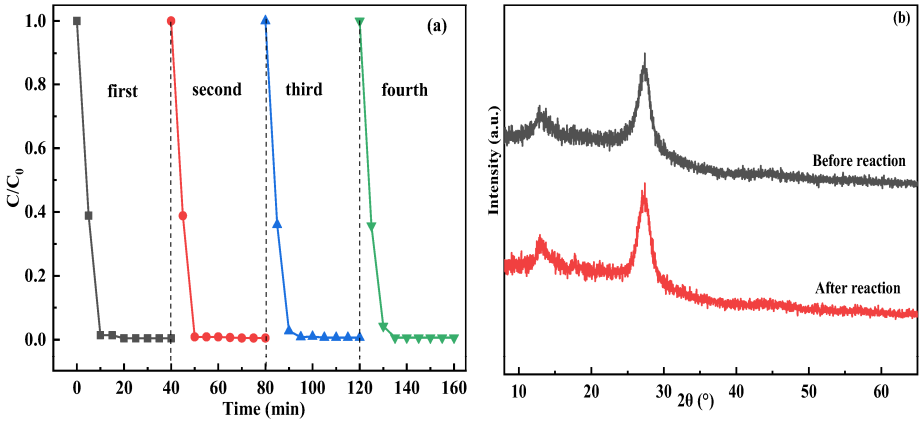

Figure 10. (**a**) Cycling experiments of the photocatalytic RhB dye degradation under visible light and (**b**) XRD patterns before and after photocatalytic RhB dye degradation for UCN.

Furthermore, the photocatalytic property of g-C_3N_4 was compared with other materials explored by other researchers in removing RhB dye, and the results are demonstrated in Table 3. Although the g-C_3N_4 studied in this work is relatively basic, its degradation rate of RhB dye exceeds that of other composite photocatalysts. The results demonstrate that g-C_3N_4 exhibits superior photocatalytic performance compared with most materials over a specific time, thereby establishing a robust foundation for further research.

Table 3. Comparison of RhB dye treatment efficiency of different photocatalysts.

Photocatalyst (Dosages)	RhB (mg/L)	Time (min)	Rate (%)	Light Source	Refs.
g-C_3N_4 (50 mg)	10	20	99.36	300 W Xe lamp	This paper
	20		99.39		
	30		99.35		
g-C_3N_4 (50 mg)	10	20	100	Direct sunlight	This paper
	20		98.78		
	30		99.15		
ZnO-g-C_3N_4 (40%)-Go (15%) (15 mg)	10	100	98	350 W Xe lamp	[63]
g-C_3N_4/$Bi_4O_5Br_2$-75 (50 mg)	10	10	92	72 W LED lamp	[64]
$TlSnI_3$/g-C_3N_4 (100 mg)	5	120	84.60	150 W Osram bulb	[65]
TiO_2/g-C_3N_4 (50 mg)	10	150	99.30	350 W Xe lamp	[66]
Co@ZnSQDs/g-C_3N_4/MWCNT (220 mg)	10	75	96	500 W halogen lamp	[67]
g-C_3N_4/ZnO/Cu_2O (50 mg)	30	100	91.4	500 W halogen lamp	[68]

3.6. Photocatalytic Mechanism

Trapping tests were conducted to study the various species implicated in photodegradation and the primarily responsible species. The primary active species of UCN photocatalytic degradation were detected by adding IPA, BQ, and SO to RhB dye as scavengers of •OH, $\bullet O_2^-$, and h^+ [43]. Figure 11 shows that the degree of removal of RhB dye (41.56%) declined significantly with the addition of BQ, while the scavenging effect of IPA (99.58%) and SO (98.53%) was weaker than that of BQ. Therefore, in the reaction process of UCN degradation of RhB dye, $\bullet O_2^-$ serves as the primary reactive species.

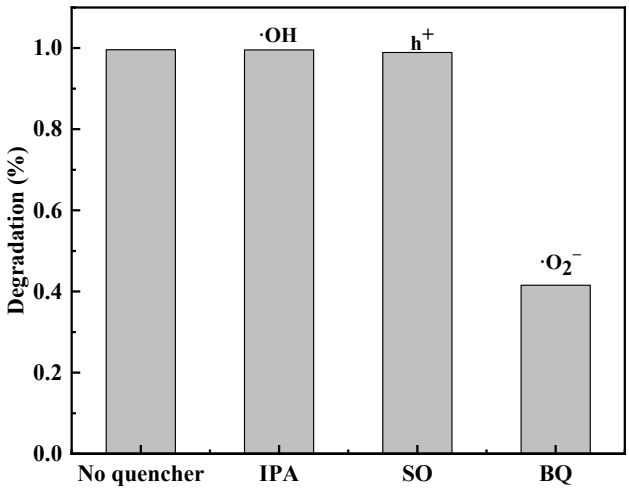

Figure 11. Trapping experiment of active species for UCN photocatalytic degradation of RhB under visible light.

The valence band (VB) potentials of a semiconductor can be determined using the empirical equation $E_{VB} = X - E^e + 0.5E_g$, where X, E^e, and E_g represent the semiconductor's electronegativity (the X value for g-C_3N_4 is 4.72 eV [69]), the energy of free electrons on the hydrogen scale (4.5 eV), and the semiconductor's bandgap, respectively [70]. Moreover, the CB potentials can be calculated using $E_{CB} = E_{VB} + E_g$ [71]. In the DRS analysis results (Figure 5b), the E_g of UCN and MCN are 2.79 and 2.70 eV, respectively. Therefore, the CB and VB potentials of UCN are calculated to be −1.17 eV (E_{CB}) and 1.62 eV (E_{VB}), while the CB and VB potentials of MCN are −1.13 eV (E_{CB}) and 1.57 eV (E_{VB}), respectively. According to these results, Figure 12 illustrates the plausible photocatalytic mechanism involved in the process of RhB photocatalytic degradation. UCN and MCN tend to produce e^- and h^+ under visible light radiation. Since the CB potential of UCN and MCN is lower than $E^\theta(O_2/\bullet O_2^-)$ = −0.33 eV, the e^- in the CB of UCN and MCN can capture the adsorbed O_2

on the catalyst surface and reduce it to give $\bullet O_2^-$. Since the E_{VB} of UCN and MCN are more negative than $E^{\theta}(\bullet OH/H_2O)$ = 2.27 eV [71], •OH cannot be generated on the VB of UCN and MCN. The results correlate with the trapping experiments.

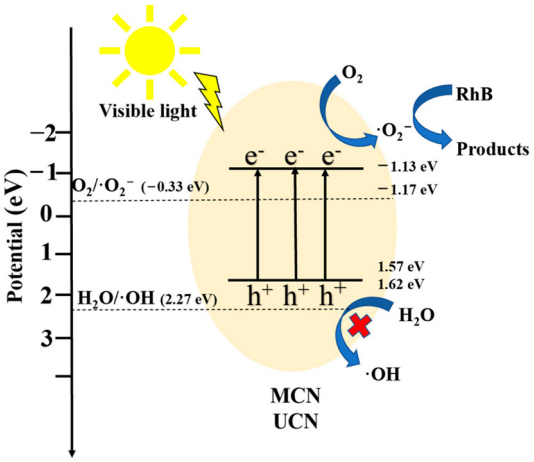

Figure 12. Photocatalytic mechanism diagram of MCN and UCN under visible light radiation.

4. Conclusions

MCN and UCN were prepared via thermal polymerisation using melamine and urea as precursors. Compared to MCN, UCN exhibits superior photocatalytic degradation performance towards RhB dye. Under the irradiation of visible light, the removal rate of RhB dye at 10 mg/L within 20 min reaches 99.36%, while complete degradation can be achieved under sunlight. The photocatalytic efficiency of UCN is enhanced by the layered structures and a large specific surface area, which enrich the reaction sites, improve the transfer of photoinduced charges, and strengthen the absorbance of visible light. The prepared UCN exhibits exceptional stability, even after undergoing four cycles of photocatalytic reaction. Moreover, the trapping experiments established that $\bullet O_2^-$ was the primary reactive species in the photocatalytic degradation of RhB dye under visible light radiation. Therefore, the as-synthesised UCN are promising photocatalysts for environmental applications such as the treatment of industrial wastewater under natural sunlight. This study highlights the potential of UCN as a photocatalyst for RhB dye removal in wastewater treatment and lays a foundation for further exploration of g-C_3N_4.

Author Contributions: Conceptualisation, software, data curation, formal analysis, writing—original draft, M.Z.; writing—review and editing, M.X., B.D., H.Z. (Hongxiang Zhu), Q.L., X.L. and J.M.; supervision, writing—review and editing, X.S. and H.Z. (Hongxia Zhang); funding acquisition, X.S. All authors have read and agreed to the published version of the manuscript.

Funding: This work was financially supported by the National Natural Science Foundation of China (No. 52070049) and the Innovation Project of Guangxi Graduate Education (No. YCSW2023354).

Data Availability Statement: Data are available upon request.

Conflicts of Interest: The authors declare no conflict of interest.

References

1. Tian, Y.; Zhang, J.; Wang, W.; Liu, J.; Zheng, X.; Li, J.; Guan, X. Facile assembly and excellent elimination behavior of porous BiOBr-g-C_3N_4 heterojunctions for organic pollutants. *Environ. Res.* **2022**, *209*, 112889. [CrossRef] [PubMed]
2. Mahdieh, V.; Iman, K.; Farzaneh, S.; Parastoo, J. Green synthesis of a novel magnetic Fe_3O_4@SiO_2/TiO_2@WO_3 nanocomposite for methylene blue removal under UV and visible light irradiations. *Res. Chem. Intermed.* **2023**, *49*, 1909–1924.
3. Zhang, M.; Sun, X.; Wang, C.; Wang, Y.; Tan, Z.; Li, J.; Xi, B. Photocatalytic degradation of rhodamine B using $Bi_4O_5Br_2$-doped ZSM-5. *Mater. Chem. Phys.* **2022**, *278*, 125697. [CrossRef]
4. Budnyak, T.M.; Onwumere, J.; Pylypchuk, I.V.; Jaworski, A.; Chen, J.; Rokicińska, A.; Lindström, M.E.; Kuśtrowski, P.; Sevastyanova, O.; Slabon, A. LignoPhot: Conversion of hydrolysis lignin into the photoactive hybrid lignin/$Bi_4O_5Br_2$/BiOBr composite for simultaneous dyes oxidation and Co^{2+} and Ni^{2+} recycling. *Chemosphere* **2021**, *279*, 130538. [CrossRef] [PubMed]

5. Li, Z.; Ma, B.; Zhang, X.; Sang, Y.; Liu, H. One-pot synthesis of BiOCl nanosheets with dual functional carbon for ultra-highly efficient photocatalytic degradation of RhB. *Environ. Res.* **2020**, *182*, 109077. [CrossRef]
6. Yang, X.; Zhang, L.; Wang, D.; Zhang, Q.; Zeng, J.; Zhang, R. Facile synthesis of nitrogen-defective g-C_3N_4 for superior photocatalytic degradation of rhodamine B. *RSC Adv.* **2021**, *11*, 30503–30509. [CrossRef] [PubMed]
7. Zhou, J.; Liu, W.; Cai, W. The synergistic effect of Ag/AgCl@ZIF-8 modified g-C_3N_4 composite and peroxymonosulfate for the enhanced visible-light photocatalytic degradation of levofloxacin. *Sci. Total Environ.* **2019**, *696*, 133962. [CrossRef] [PubMed]
8. Cui, S.; Li, X.; Li, Y.; Zhao, H.; Wang, Y.; Li, N.; Li, X.; Li, G. Synthesis of CdS/m-TiO_2 mesoporous spheres and their application in photocatalytic degradation of rhodamine B under visible light. *Chem. Res. Chin. Univ.* **2017**, *33*, 436–441. [CrossRef]
9. Wang, C.; Sun, X.; Zhang, M.; Wang, Y.; Tan, Z.; Li, J.; Xi, B. Ultrasound-assisted room-temperature in situ precipitation synthesis of BC doped $Bi_4O_5Br_2$ for enhanced photocatalytic activity in pollutants degradation under visible light. *J. Alloys Compd.* **2021**, *889*, 161609. [CrossRef]
10. Zhang, G.-Q.; Chang, N.; Han, D.-Q.; Zhou, A.-Q.; Xu, X.-H. The enhanced visible light photocatalytic activity of nanosheet-like Bi_2WO_6 obtained by acid treatment for the degradation of rhodamine B. *Mater. Lett.* **2010**, *64*, 2135–2137. [CrossRef]
11. Hu, C.; Xu, M.; Zhang, J.; Zhou, Y.; Hu, B.; Yu, G. Recyclable MoO_3 nanobelts for photocatalytic degradation of Rhodamine B by near infrared irradiation. *Int. J. Chem. Kinet.* **2018**, *51*, 3–13. [CrossRef]
12. Nguyen, L.T.T.; Vo, D.-V.N.; Nguyen, L.T.H.; Duong, A.T.T.; Nguyen, H.Q.; Chu, N.M.; Nguyen, D.T.C.; Van Tran, T. Synthesis, characterization, and application of $ZnFe_2O_4$@ZnO nanoparticles for photocatalytic degradation of Rhodamine B under visible-light illumination. *Environ. Technol. Innov.* **2021**, *25*, 102130. [CrossRef]
13. Lin, X.; Li, Y. Preparation of TiO_2/Ag[BMIM]Cl Composites and Their Visible Light Photocatalytic Properties for the Degradation of Rhodamine B. *Catalysts* **2021**, *11*, 661. [CrossRef]
14. Liu, W.; Li, Y.; Liu, F.; Jiang, W.; Zhang, D.; Liang, J. Visible-light-driven photocatalytic degradation of diclofenac by carbon quantum dots modified porous g-C_3N_4: Mechanisms, degradation pathway and DFT calculation. *Water Res.* **2018**, *151*, 8–19. [CrossRef] [PubMed]
15. Prabavathi, S.L.; Saravanakumar, K.; Mamba, G.; Muthuraj, V. 1D/2D $MnWO_4$ nanorods anchored on g-C_3N_4 nanosheets for enhanced photocatalytic degradation ofloxacin under visible light irradiation. *Colloids Surf. A. Physicochem. Eng. Asp.* **2019**, *581*, 123845.
16. Song, Y.; Gu, J.; Xia, K.; Yi, J.; Che, H.; She, X.; Chen, Z.; Ding, C.; Li, H.; Xu, H. Construction of 2D SnS_2/g-C_3N_4 Z-scheme composite with superior visible-light photocatalytic performance. *Appl. Surf. Sci.* **2019**, *467/468*, 56–64. [CrossRef]
17. Orooji, Y.; Ghanbari, M.; Amiri, O.; Salavati-Niasari, M. Facile fabrication of silver iodide/graphitic carbon nitride nanocomposites by notable photo-catalytic performance through sunlight and antimicrobial activity. *J. Hazard. Mater.* **2020**, *389*, 122079. [CrossRef] [PubMed]
18. Li, H.; Wang, Z.; Lu, Y.; Liu, S.; Chen, X.; Wei, G.; Ye, G.; Chen, J. Microplasma electrochemistry (MIPEC) methods for improving the photocatalytic performance of g-C_3N_4 in degradation of RhB. *Appl. Surf. Sci.* **2020**, *531*, 147307. [CrossRef]
19. Yang, Z.; Zhang, Y.; Schnepp, Z. Soft and hard templating of graphitic carbon nitride. *J. Mater. Chem. A* **2015**, *3*, 14081–14092. [CrossRef]
20. Wang, W.; Li, G.; An, T.; Chan, D.K.L.; Yu, J.C.; Wong, P.K. Photocatalytic hydrogen evolution and bacterial inactivation utilizing sonochemical-synthesized g-C_3N_4/red phosphorus hybrid nanosheets as a wide-spectral-responsive photocatalyst: The role of type I band alignment. *Appl. Catal. B Environ.* **2018**, *238*, 126–135. [CrossRef]
21. Zhong, S.; Zhou, H.; Shen, M.; Yao, Y.; Gao, Q. Rationally designed a g-C_3N_4/BiOI/$Bi_2O_2CO_3$ composite with promoted photocatalytic activity. *J. Alloys Compd.* **2021**, *853*, 157307. [CrossRef]
22. Cao, C.; Wang, H. Carbon nitride films deposited from organic solutions by electrodeposition. *Diam. Relat. Mater.* **1999**, *8*, 1786–1789. [CrossRef]
23. Viehland, J.; Lin, S.; Feldman, B.J.; Kilgore, K.; Jones, M.T. Search for the nitrogen dangling bond in amorphous hydrogenated carbon nitride. *Solid State Commun.* **1991**, *80*, 597–599. [CrossRef]
24. Wei, H.; McMaster, W.A.; Tan, J.Z.Y.; Cao, L.; Chen, D.; Caruso, R.A. Mesoporous TiO_2/g-C_3N_4 Microspheres with Enhanced Visible-Light Photocatalytic Activity. *J. Phys. Chem. C. Nanomater. Interfaces* **2017**, *121*, 22114–22122. [CrossRef]
25. Bai, Y.-J.; Lü, B.; Liu, Z.-G.; Li, L.; Cui, D.-L.; Xu, X.-G.; Wang, Q.-L. Solvothermal preparation of graphite-like C_3N_4 nanocrystals. *J. Cryst. Growth* **2003**, *247*, 505–508. [CrossRef]
26. Niu, P.; Zhang, L.; Liu, G.; Cheng, H.-M. Graphene-Like Carbon Nitride Nanosheets for Improved Photocatalytic Activities. *Adv. Funct. Mater.* **2012**, *22*, 4763–4770. [CrossRef]
27. Andreyev, A.; Akaishi, M.; Golberg, D. Sodium flux-assisted low-temperature high-pressure synthesis of carbon nitride with high nitrogen content. *Chem. Phys. Lett.* **2003**, *372*, 635–639. [CrossRef]
28. Goettmann, F.; Fischer, A.; Antonietti, M.; Thomas, A. Chemical Synthesis of Mesoporous Carbon Nitrides Using Hard Templates and Their Use as a Metal-Free Catalyst for Friedel-Crafts Reaction of Benzene. *Angew. Chem.* **2006**, *45*, 4467–4471. [CrossRef] [PubMed]
29. Zhang, J.; Guo, F.; Wang, X. An Optimized and General Synthetic Strategy for Fabrication of Polymeric Carbon Nitride Nanoarchitectures. *Adv. Funct. Mater.* **2013**, *23*, 3008–3014. [CrossRef]
30. Yan, S.C.; Li, Z.S.; Zou, Z.G. Photodegradation Performance of g-C_3N_4 Fabricated by Directly Heating Melamine. *Langmuir* **2009**, *25*, 10397–10401. [CrossRef] [PubMed]

31. Liu, J.; Zhang, T.; Wang, Z. Simple pyrolysis of urea into graphitic carbon nitride with recyclable adsorption and photocatalytic activity. *J. Mater. Chem. A* **2011**, *21*, 14398–14401. [CrossRef]
32. Ma, Y.; Liu, E.; Hu, X.; Tang, C.; Wan, J.; Li, J.; Fan, J. simple process to prepare few-layer g-C_3N_4 nanosheets with enhanced photocatalytic activities. *Appl. Surf. Sci.* **2015**, *358*, 246–251. [CrossRef]
33. Dong, L.; Chunling, L.; Jiayu, G.; Congyue, Z.; Qian, Z.; Fengquan, Z.; Tianjun, N.; Weidong, W. 3D interconnected g-C_3N_4 hybridized with 2D Ti_3C_2 MXene nanosheets for enhancing visible light photocatalytic hydrogen evolution and dye contaminant elimination. *Appl. Surf. Sci.* **2021**, *579*, 152180.
34. Xu, F.; Cheng, G.; Song, S.; Wei, Y.; Chen, R. Insights into Promoted Adsorption Capability of Layered BiOCl Nanostructures Decorated with TiO_2 Nanoparticles. *ACS Sustain. Chem. Eng.* **2016**, *4*, 12. [CrossRef]
35. Xiong, J.; Gan, Y.; Zhu, J.; Li, W.; Gao, C.; Wei, Y.; Cheng, G.; Li, Z.; Dou, S. Insights into the structure-induced catalysis dependence of simply engineered one-dimensional zinc oxide nanocrystals towards photocatalytic water purification. *Inorg. Chem. Front.* **2017**, *4*, 2075–2087. [CrossRef]
36. Zhang, M.; Xiong, J.; Yang, H.; Wen, Z.; Chen, R.; Cheng, G. Surface Potential/Wettability and Interface Charge Transfer Engineering of Copper-Oxide (Cu–MOx, M = W, Ti, and Ce) Hybrids for Efficient Wastewater Treatment through Adsorption–Photocatalysis Synergy. *Ind. Eng. Chem. Res.* **2020**, *59*, 35. [CrossRef]
37. Luo, Y.; Wei, X.; Gao, B.; Zou, W.; Zheng, Y.; Yang, Y.; Zhang, Y.; Tong, Q.; Dong, L. Synergistic adsorption-photocatalysis processes of graphitic carbon nitrate (g-C_3N_4) for contaminant removal: Kinetics, models, and mechanisms. *Chem. Eng. J.* **2019**, *375*, 122019. [CrossRef]
38. Yu, Y.; Chen, D.; Xu, W.; Fang, J.; Sun, J.; Liu, Z.; Chen, Y.; Liang, Y.; Fang, Z. Synergistic adsorption-photocatalytic degradation of different antibiotics in seawater by a porous g-C_3N_4/calcined-LDH and its application in synthetic mariculture wastewater. *J. Hazard. Mater.* **2021**, *416*, 126183. [CrossRef]
39. Ni, T.; Zhang, H.; Yang, Z.; Zhou, L.; Pan, L.; Li, C.; Yang, Z.; Liu, D. Enhanced adsorption and catalytic degradation of antibiotics by porous 0D/3D Co_3O_4/g-C_3N_4 activated peroxymonosulfate: An experimental and mechanistic study. *J. Colloid Interface Sci.* **2022**, *625*, 466–478. [CrossRef] [PubMed]
40. Liu, D.; Li, C.; Zhao, C.; Zhao, Q.; Niu, T.; Pan, L.; Xu, P.; Zhang, F.; Wu, W.; Ni, T. Facile synthesis of three-dimensional hollow porous carbon doped polymeric carbon nitride with highly efficient photocatalytic performance. *Chem. Eng. J.* **2022**, *438*, 135623. [CrossRef]
41. Wang, Y.; Cao, Y.; Liu, Y.; Yang, P. Effect of nonmetal element dopants on photo- and electro-chemistry performance of ultrathin g-C_3N_4 nanosheets. *Int. J. Hydrogen Energy* **2020**, *45*, 16519–16527. [CrossRef]
42. Di, X.; Shuo, Z.; Tianyu, W.; Mei, H.; Yiyan, C.; Panpan, Z.; Fangchao, C. Efficient RhB degradation using $MnFe_2O_4$/g-C_3N_4 composites under visible light irradiation. *Opt. Mater.* **2022**, *124*, 111965.
43. Zhang, M.; Xing, M.; Dong, B.; Sun, X.; Zhang, H.; Wang, C.; Zhu, H. Preparation of $BiVO_4/CO_3^{2-}$-$Bi_2O_2CO_3$ heterojunctions for enhanced photocatalytic activity in the degradation of levofloxacin under visible light. *J. Alloys Compd.* **2023**, *965*, 171471. [CrossRef]
44. Minjie, Z.; Aiyue, J.; Yujuan, C.; Mengyu, T.; Yulian, W.; Zhigang, T. Synergistic effects of Au/g-C_3N_4/montmorillonite composite nanocatalysts for enhanced photocatalytic performance with visible light illumination. *J. Nanoparticle Res.* **2023**, *25*, 87.
45. Li, D.; Huang, J.; Li, R.; Chen, P.; Chen, D.; Cai, M.; Liu, H.; Feng, Y.; Lv, W.; Liu, G. Synthesis of a carbon dots modified g-C_3N_4/SnO_2 Z-scheme photocatalyst with superior photocatalytic activity for PPCPs degradation under visible light irradiation. *J. Hazard. Mater.* **2021**, *401*, 123257.1–123257.13. [CrossRef] [PubMed]
46. Van, K.N.; Huu, H.T.; Nguyen Thi, V.N.; Le Thi, T.L.; Truong, D.H.; Truong, T.T.; Dao, N.N.; Vo, V.; Tran, D.L.; Vasseghian, Y. Facile construction of S-scheme SnO_2/ g-C_3N_4 photocatalyst for improved photoactivity. *Chemosphere* **2021**, *289*, 133120. [CrossRef]
47. Ghafuri, H.; Rashidizadeh, A.; Zaron, T.M. Facile preparation of CuS-g-C_3N_4/Ag nanocomposite with improved photocatalytic activity for the degradation of rhodamine B. *Polyhedron* **2020**, *179*, 114368. [CrossRef]
48. Ma, W.; Wang, N.; Guo, Y.; Yang, L.; Lv, M.; Tang, X.; Li, S. Enhanced photoreduction CO_2 activity on g-C_3N_4: By synergistic effect of nitrogen defective-enriched and porous structure, and mechanism insights. *Chem. Eng. J.* **2020**, *388*, 124288. [CrossRef]
49. Zhu, Z.; Fan, W.; Liu, Z.; Yu, Y.; Dong, H.; Huo, P.; Yan, Y. Fabrication of the metal-free biochar-based graphitic carbon nitride for improved 2-Mercaptobenzothiazole degradation activity. *J. Photochem. Photobiol. A Chem.* **2018**, *358*, 284–293. [CrossRef]
50. Xu, Z.; Zhang, J.; Zhong, J.; Wu, J.; Li, M. Reductively-induced carbon vacancies facilitate visible light-driven hydrogen evolution enhancement of g-C_3N_4. *Mater. Sci. Semicond. Process.* **2023**, *161*, 107459. [CrossRef]
51. Shi, J.; Chen, T.; Guo, C.; Liu, Z.; Feng, S.; Li, Y.; Hu, J. The bifunctional composites of AC restrain the stack of g-C_3N_4 with the excellent adsorption-photocatalytic performance for the removal of RhB. *Colloids Surf. A. Physicochem. Eng. Asp.* **2019**, *580*, 123701. [CrossRef]
52. Bai, J.; Yin, C.; Xu, H.; Chen, G.; Ni, Z.; Wang, Z.; Li, Y.; Kang, S.; Zheng, Z.; Li, X. Facile urea-assisted precursor pre-treatment to fabricate porous g-C_3N_4 nanosheets for remarkably enhanced visible-light-driven hydrogen evolution. *J. Colloid Interface Sci.* **2018**, *532*, 280–286. [CrossRef] [PubMed]
53. Zhu, J.; Xiong, Y.; Mu, X.; Wan, J.; Li, T.; Jin, Y.; Li, R. Cobalt-Doped g-C_3N_4 Nanosheets for One-Pot Synthesis of Imines under Mild Conditions. *ACS Appl. Nano Mater.* **2023**, *6*, 7. [CrossRef]

54. Guo, Y.; Li, C.; Guo, Y.; Wang, X.; Li, X. Ultrasonic-assisted synthesis of mesoporous g-C_3N_4/Na-bentonite composites and its application for efficient photocatalytic simultaneous removal of Cr(VI) and RhB. *Colloids Surf. A. Physicochem. Eng. Asp.* **2019**, *578*, 123624. [CrossRef]
55. Liu, X.; Pang, F.; He, M.; Ge, J. Confined reaction inside nanotubes: New approach to mesoporous g-C_3N_4 photocatalysts. *Nano Res.* **2017**, *10*, 3638–3647. [CrossRef]
56. Liqun, Y.; Xiaoli, J.; Chuan, L.; Chenghua, D.; Haiquan, X.; Ka Him, C.; Po Keung, W. Thickness-ultrathin and bismuth-rich strategies for BiOBr to enhance photoreduction of CO_2 into solar fuels. *Appl. Catal. B Environ.* **2016**, *187*, 281–290.
57. Feng, W.; Fang, J.; Zhou, G.; Zhang, L.; Lu, S.; Wu, S.; Chen, Y.; Ling, Y.; Fang, Z. Rationally designed Bi@BiOCl/g-C_3N_4 heterostructure with exceptional solar-driven photocatalytic activity. *Mol. Catal.* **2017**, *434*, 69–79. [CrossRef]
58. Hong, Y.; Li, C.; Zhang, G.; Meng, Y.; Yin, B.; Zhao, Y.; Shi, W. Efficient and stable Nb_2O_5 modified g-C_3N_4 photocatalyst for removal of antibiotic pollutant. *Chem. Eng. J.* **2016**, *299*, 74–84. [CrossRef]
59. Wang, J.; Yang, Z.; Gao, X.; Yao, W.; Wei, W.; Chen, X.; Zong, R.; Zhu, Y. Core-shell g-C_3N_4@ZnO composites as photoanodes with double synergistic effects for enhanced visible-light photoelectrocatalytic activities. *Appl. Catal. B* **2017**, *217*, 169–180. [CrossRef]
60. Pei, Q.; Mengjie, L.; Gang, C.; Wei, L.; Lijun, L.; Jinyan, X. Co-implantation of oxygen vacancy and well-dispersed Cu cocatalyst into TiO_2 nanoparticles for promoting solar-to-hydrogen evolution. *Int. J. Hydrogen Energy* **2022**, *48*, 933–942.
61. Chen, X.; Yao, L.; He, J.; Li, J.; Xu, S.; Li, N.; Zhu, Y.; Chen, X.; Zhu, R. Enhanced degradation of tetracycline under natural sunlight through the synergistic effect of Ag_3PO_4/MIL-101(Fe) photocatalysis and Fenton catalysis: Mechanism, pathway, and toxicity assessment. *J. Hazard. Mater.* **2023**, *449*, 131024. [CrossRef]
62. Guo, H.; Niu, C.-G.; Wen, X.-J.; Zhang, L.; Liang, C.; Zhang, X.-G.; Guan, D.-L.; Tang, N.; Zeng, G.-M. Construction of highly efficient and stable ternary AgBr/Ag/$PbBiO_2Br$ Z-scheme photocatalyst under visible light irradiation: Performance and mechanism insight. *J. Colloid Interface Sci.* **2017**, *513*, 852–865. [CrossRef]
63. Zhang, J.; Li, J.; Liu, X. Ternary nanocomposite ZnO- g-C_3N_4–Go for enhanced photocatalytic degradation of RhB. *Opt. Mater.* **2021**, *119*, 111351. [CrossRef]
64. Yi, F.; Ma, J.; Lin, C.; Wang, L.; Zhang, H.; Qian, Y.; Zhang, K. Insights into the enhanced adsorption/photocatalysis mechanism of a $Bi_4O_5Br_2$/g-C_3N_4 nanosheet. *J. Alloys Compd.* **2020**, *821*, 153557. [CrossRef]
65. Fatemeh, Y.; Qahtan, A.Y.; Mojgan, G.; Masoud, S.-N. Fabrication of $TlSnI_3$/C_3N_4 nanocomposites for enhanced photodegradation of toxic contaminants below visible light and investigation of kinetic and mechanism of photocatalytic reaction. *J. Mol. Liq.* **2022**, *349*, 118443.
66. Jiang, Z.; Zhu, C.; Wan, W.; Qian, K.; Xie, J. Constructing graphite-like carbon nitride modified hierarchical yolk–shell TiO_2 spheres for water pollution treatment and hydrogen production. *J. Mater. Chem. A* **2015**, *4*, 1806–1818. [CrossRef]
67. Danish, M.; Muneer, M. Facile synthesis of highly efficient Co@ZnSQDs/g-C_3N_4/MWCNT nanocomposites and their photocatalytic potential for degradation of RhB dye: Efficiency, degradation kinetics, and mechanism pathway. *Ceram. Int.* **2021**, *47*, 13043–13056. [CrossRef]
68. Renji, R.; Shanmugam, V.; Asokan, S.; Palanisamy, P.; Sanjeevamuthu, S.; Vairamuthu, R.; Jeyaperumal Kalyana, S.; Manickam, S.; Mohd, S.; AlFaify, S. Investigation on novel Cu_2O modified g-C_3N_4/ZnO heterostructures for efficient photocatalytic dye degradation performance under visible-light exposure. *Colloid Interface Sci. Commun.* **2021**, *44*, 100480.
69. Luo, J.; Zhou, X.; Ma, L.; Xu, X. Enhancing visible-light photocatalytic activity of g-C_3N_4 by doping phosphorus and coupling with CeO_2 for the degradation of methyl orange under visible light irradiation. *RSC Adv.* **2015**, *5*, 68728–68735. [CrossRef]
70. Zhang, L.; Wang, G.; Xiong, Z.; Tang, H.; Jiang, C. Fabrication of flower-like direct Z-scheme beta-Bi_2O_3/g-C_3N_4 photocatalyst with enhanced visible light photoactivity for Rhodamine B degradation. *Appl. Surf. Sci.* **2018**, *436*, 162–171. [CrossRef]
71. Huang, L.; Liu, J.; Li, P.; Li, Y.; Wang, C.; Shu, S.; Song, Y. CQDs modulating Z-scheme g-C_3N_4/BiOBr heterostructure for photocatalytic removing RhB, BPA and TC and E. coli by LED light. *J. Alloys Compd.* **2022**, *895*, 162637. [CrossRef]